From –20 to 200 °C: Fuel Cells with Broad Operational Flexibility Enabled by Intrinsically Ultramicroporous Membranes

Hongying Tang
Tianjin Nomal University
Kang Geng
Institute of Coal Chemistry, Chinese Academy of Sciences
Lei Wu
Institute of Coal Chemistry, Chinese Academy of Sciences
Junjie Liu
Hubei Nuclear Solid Physics Key Laboratory, Department of Physics, Wuhan University
Zhiquan Chen
Hubei Nuclear Solid Physics Key Laboratory, Department of Physics, Wuhan University
Wei You
Engineering Plastics, Institute of Chemistry, Chinese Academy of Sciences
Feng Yan
College of Chemistry, Chemical Engineering and Materials Science, Soochow University
Michael D. Guiver
State Key Laboratory of Engines, Tianjin University
Nanwen Li (linanwen@sxicc.ac.cn)
Institute of Coal Chemistry, Chinese Academy of Sciences

Article

Keywords: Proton exchange membrane, fuel cell, Proton conductivity, Cold start-up, Intrinsic ultramicroporosity

Posted Date: May 21st, 2021

DOI: https://doi.org/10.21203/rs.3.rs-506290/v1

Version of Record: A version of this preprint was published at Nature Energy on January 3rd, 2022. See the published version at https://doi.org/10.1038/s41560-021-00956-w.

Abstract

Conventional proton exchange membrane fuel cells (PEMFCs) operate at a narrow temperature range, either under low temperature conditions (80–90°C) using fully-humidified perfluorosulfonic acid (Nafion®) membranes or under non-humidified high temperature conditions (140–180°C) using phosphoric acid (PA)-doped membranes to avoid water condensation-induced PA leaching. To allow wide operational flexibility over the full spectrum of temperature and humidity ranges, we present an innovative design strategy by using PA-doped intrinsically ultramicroporous membranes constructed from rigid and contorted high free volume polymers. The membranes with an average ultramicropore radius of 3.3 Å showed a significant siphoning effect as confirmed by the delocalization of PA in ^{31}P NMR, thus allowing high retention of PA even under highly humidified conditions and presenting more than three orders of magnitude higher proton conductivity retention than conventional dense PA-doped polybenzimidazole membranes (PBI/PA). The resulting PEMFCs display impressive performance over a much broader temperature range from − 20 to 200°C and can accomplish over 100 start-up/shut-down cycles even at − 20°C. The broad operational flexibility rendered from the high PA-retention can ultimately simplify heat and water management and thereby reduce PEMFC costs.

Introduction

Proton exchange membrane fuel cells (PEMFCs) have been applied in numerous portable and stationary applications due to their high power density and minimal pollution.[1] The two conventional types of hydrogen PEMFCs, which are low temperature PEMFCs using perfluorosulfonic acid (PFSA) polyelectrolytes (*e.g.*, Nafion®) and high temperature PEMFCs using phosphoric acid-doped polyelectrolytes (*e.g.*, polybenzimidazole (PBI/PA)), each have their advantages and limitations. PFSA-based PEMFCs have been commercialized for vehicles, as they have excellent proton conductivity under fully humidified conditions at relatively low temperatures (~ 80 °C). As relative humidity (RH) decreases, sulfonated proton exchange membranes (PEMs) become much less conductive, and eventually dehydrate. In commercial PEMFC usage for vehicles using conventional PEMs, water and heat management, such as the need for large radiators to dissipate waste heat, are required.[2,3] In contrast, acid-base type PEMFCs operate at temperatures above 140 °C and typically do not require humidification or heat management systems. A higher operating temperature enhances electrocatalyst reactivity, and increases tolerance to CO or H_2S contaminants in hydrogen inlet streams (>1% CO at 150 °C).[4-7] Although PEMFCs based on PBI/PA membranes can operate reliably at 160 °C without additional humidification for over 27,000 hours, the water-soluble PA doped into the membrane leaches out when humidity is present under cold start-up or/and frequent start-up/shut-down cycles, which limits the fuel cell function below 140 °C.[8-14] Thus, broadening the operation temperature and RH windows, and further achieving sub-zero start-up capabilities become the critical challenges for the commercialization of high temperature (HT) PEMFC systems.[15-18]

At present, common strategies to improve cold-start-up performance depend on engineering means and external assistance to manage water during shut-down and start-up, such as using a 3D fine mesh cathode flow channel, introducing gas purging procedures, installing an additional internal/external heating device, or including an alternate hydrogen pump.[16,18-20] However, improving PEM proton conductivity below 0 °C, which seems like a straightforward strategy to solve cold-start-up challenges, has rarely been applied in low-temperature PEMFCs. Since PA-doped PEMs do not rely on water to transport protons, it is reasonable to hypothesize that PA-doped PEMFCs could start-up and operate below 0 °C, if a solution to the intractable problem of how to prevent PA leaching under low temperature conditions is found.

The key to PA leaching with water absorption/desorption in HT PEMs is believed to be because of weaker interactions of PA in the PBI matrix. To address this, the introduction of stronger basicity to form quaternary ammonium-biphosphate ion pairs (QAPOH) has resulted in strong PA interactions in HT PEMs.[21-24]. This strategy of strong ion-pairs interactions significantly decreased PEM PA loss in the presence of water, and the resulting PEMFCs exhibited stable performance at 80 °C, which

was significantly lower than conventional PA-doped PBI PEMFCs. However, these QAPOH-based PEMFCs have not been explored to operate at temperatures lower than 80 °C, nor at sub-zero temperatures, without suffering the loss of PA.

Here, we firstly demonstrate that HT PEMFCs based on intrinsically microporous polymers strongly mitigate PA leaching and thus overcome the limitations of conventional PBI-based fuel cells. In the tunable subnanometer-level intrinsic microporosity of polymers derived from Tröger's base, a V-shaped bridged bicyclic diamine, both the siphoning effect of micropososity and the acid-base interactions with PA are proposed to synergistically support unprecedented PA retention and efficient proton conduction in PEMFCs.[25-35] These outstanding properties enable PEMFC operation under a wide range of conditions at temperatures from −20 to 200 °C without external humidification, allowing multiple start up and shut down cycles, which is far beyond existing technologies.

Results

Polymer Intrinsic Microporosity

Four high molecular weight TB-based polymers (*i.e.*, dimethyldiphenylmethane (DMDPM-TB), dimethylbiphenyl (DMBP-TB), trimethylphenylindan (TMPI-TB), and triptycene (Trip-TB) were prepared (Figure 1a, Figure S1, and Table S1). The four polymers were designed to elicit variations in the intrinsic micropore size and distribution through differences in steric hindrance, rotational flexibility, and packing efficiency of the polymer chains.[27,36] Ultra/microporosity characterization employed positron annihilation lifetime spectroscopy (PALS), which is based on lifetime measurements of γ-ray-generated positronium located in material free volumes.[37] The peak-normalized PALS spectra of the four TB films covering a broad channel number from around 1000 to 2400 were analyzed by both PATFIT and CONTIN programs (Figure 1b, Figure S2, and Table S2).[38,39] As shown in Table 1, the average radius (R_3) of the spherical pores correlating to the triplet positronium (*o*-Ps) third mean lifetime (t_3), their corresponding relative intensities (I_3), and the corresponding relative fractional free volume (FFV_3) within the films were determined by semi-empirical equations using the finite-term lifetime analysis PATFIT program.[39] The three DMDPM-TB, DMBP-TB, and TMPI-TB membranes exhibited one kind of ultramicrocavity with $R_3 < 3.5$ Å, while the Trip-TB had two *o*-Ps components indicating two kinds of microcavities ($t_3/I_3/R_3/FFV_3$ and $t_4/I_4/R_4/FFV_4$ correlating to the third and fourth mean lifetime, respectively), which is likely due to the internal free volume elements the triptycene structures disrupting the polymer chain packing. The small-sized microcavities in Trip-TB have an average radius of 2.8 Å (R_3), which is dominant by the annihilation intensity, although the FFV_3 is less than half of FFV_4. Among the four TB-based films, DMBP-TB and Trip-TB have the largest overall FFV, and a 3D modelled structure of DMBP-TB in an amorphous cell is also provided in Figure 1c.

Table 1. The properties of the TB polymers and PA-doped TB membranes.

Membranes	Before PA Doping					After PA Doping			After washing by DI water	
	t_3 [ns][a]	I_3 [%][a]	R_3 [Å][a]	FFV_3 [%][a]	S_{BET} [m^2/g][d]	S_{BET} [m^2/g][d]	PA uptake [%][e]	ADL[f]	S_{BET} [m^2/g][d]	ADL retention
***m*-PBI**	--[b]	--[b]	--[b]	--[b]	--[b]	--[b]	333	10.5	--[b]	44.2%
DMDPM-TB	1.94	17.62	2.8	29	4	--[g]	--[g]	--[g]	--[g]	--[g]
DMBP-TB	2.51	19.24	3.3	52	301	0	425	10.7	16	72.5%
TMPI-TB	2.70	10.01	3.4	30	327	19	240	7.5	15	58.0%
Trip-TB	1.95 (4.33)[c]	15.65 (9.16)[c]	2.8 (4.4)[c]	26 (59)[c]	868	275	194	6.3	778	49.2%

[a] Cavity size and distribution characterization obtained via PATFIT program from PALS. [b] Lack of microporous structure and the values could not be tested. [c] The results for the second microcavity, which are derived from the fourth mean lifetime (t_4), are provided in parentheses. [d] N_2 adsorption isotherms at 77 K of the powdered form of the polymers. [e] PA doping weight percentage determined by acid-base titration. [f] Acid doping level (mole ratio of PA and repeating unit) determined by acid-base titration. [g] The membrane was soluble in PA and the values could not be tested.

We were also curious about the microporous structures of TB-based polymers after doping with PA. However, the PALS technique cannot be applied to analyze PA-doped membranes due to contamination of the ^{22}Na source by PA. Therefore, we used the apparent Brunauer–Emmett–Teller (BET) surface areas (S_{BET}) from N_2 adsorption/desorption isotherms collected at 77 K to characterize the microporosity both before and after PA-doping (Table 1 and Figure S3). However, it is noteworthy that gas sorption measurements cannot completely elucidate the critical ultramicropore size distribution responsible for molecular sieving.[40] DMDPM-TB, which has the most polymer chain flexibility among the four TB-based polymers, was soluble in 85% PA, so that its BET measurement after PA-doping could not be performed and the membrane was unsuitable for PA-doped PEM applications. For the DMBP-TB and TMPI-TB membranes, the values of S_{BET} decreased to almost 0 after PA-doping, suggesting that the micropores were filled with PA. More interestingly, the Trip-TB showed a reduction in S_{BET} surface area from 868 to 275 $m^2\ g^{-1}$, suggesting that 32% of microporous volume was unoccupied. This is in good agreement with the PALS analysis, as the FFV of the smaller porosity (R_3 = 2.8 Å, FFV_3) was 31% of the overall FFV of Trip-TB (Table 1). This likely indicates that PA could more readily occupy bigger pores R_4 (4.4 Å) but was less able to do so in the smaller pores R_3 (2.8 Å) due to backbone rigidity. This may be the reason for the smaller acid doping level (ADL) of Trip-TB than DMBP-TB and TMPI-TB, despite its larger FFV. Furthermore, the PA absorption of TMPI-TB was about 56% of that of DMBP-TB (Table 1), which is consistent with their FFV_3 ratio (57%). Besides microporosity, we found that the rigid bicyclic tertiary amine centers in TB-based membranes appear to be critical motifs for PA absorption, as we observed little PA uptake for the prototypical intrinsic microporous membrane PIM-1 (R = 4.1 and 2.7 Å, PA uptake = 5%, Figure S4).[25]

Siphoning Effect of Ultramicroporous Membranes

The siphoning effect of microporosity to PA could be confirmed by ^{31}P NMR spectroscopy due to the delocalization of the PA signal in the micropore. In comparison to free PA (85.0% PA, 0 ppm), two types of situations are proposed: (1) when the tertiary amine in TB is protonated by PA to form $N–H^+\cdots H_2PO_4^-$ interactions, the phosphorous signal would have a downfield shift due to the electron withdrawing effect;[23] (2) the PA molecules located in the submicropores would have an negative chemical shift than free PA due to the ring current effect resulting from delocalized aromatic ring electron systems in these polymers.[35,41-46] Therefore, ^{31}P NMR spectra of TB/PA membranes with different ADLs were measured in DMSO-d_6. As shown in Figure 2, when ADL = 2, PA fully protonated the TB units and downfield chemical shifts were observed compared with free PA, except for Trip-TB, which might derive from greater steric hindrance and a more rigid polymer backbone. Both Mulliken and natural population analysis suggests that the DMBP-TB unit has the strongest Lewis basicity (Figure S5, Table S3-S5), which is consistent with its highest ^{31}P NMR chemical shift with 2 equivalent PA (Figure 2). When ADLs were saturated, a distinct signature of pore occupation was observed in the ^{31}P NMR spectrum. All TB-based membranes showed single upfield chemical shifts comparing to the free PA with no signal of bulk phosphoric acid or phosphate. The entire PA tends easily to penetrate the micropores in the TB systems after a doping process, which matches well with the analysis of the apparent BET surface areas. As a control experiment, *m*-PBI/PA without intrinsic micropores showed almost no negative chemical shift. The presence of the shoulder around 0 ppm indicated the existing of bulk free phosphoric acid in the system. Among all the tested membranes, the negative chemical shift of ^{31}P depends the micropore size and the interaction of the micropores with phosphoric acid. DMBP-TB/PA showed the highest upfield chemical shift is due to the smallest micropores. The reduced average distance between the micropore wall and PA in DMBP-TB membranes indicated the strongest spatial interactions with PA. Moreover, with the increasing PA loading, the PA penetration inside the

micropores increase, thus leading to an increase of negative chemical shift. A similar phenomenon has also been observed in the solid-state ^{31}P NMR analysis (Figure S6), further suggesting the delocalization of PA in micropore resulting from the siphoning effect of membranes with microporosity. The ^{31}P NMR chemical shift change of PA in TB/PA micropores are consistent with a recent report of PA distribution in porous electrocatalysts,[35] and it is hypothesized that both the capillary force in spatially confined micropores and the acid-base interactions play important roles in retaining PA when water is present.[33,34] Therefore, both the microporosity evaluation and the ^{31}P NMR analysis suggest that large fractional free volume (FFV_3) resulting from appropriate micropores ($R_3 \approx 3.3$ Å) are beneficial for PA absorption and retention.

To further confirm the siphoning effect of microporosity to the PA, the apparent BET surface areas of the TB membranes were obtained after soaking the TB/PA membranes three times in distilled water (each time for 12 h) at 40 ^{o}C to remove the doped PA. As shown in Table 1, the apparent BET surface areas of DMBP-TB and TMPI-TB membranes were only 16 and 15 $m^2\ g^{-1}$ respectively after the PA removal process. These values are almost close to those of the pristine PA-doped DMBP-TB and TMPI-TB membranes. In contrast, the Trip-TB membrane having the larger pore size showed significant BET recovery after PA removing. These results indicate that the intrinsic micropores having an average ultramicropore radius of 3.3-3.4 Å showed the strongest siphoning interaction with PA. Thus, the DMBP-TB membrane displayed the largest ADL-retention value of 72.5 %, which is much better than that of the *m*-PBI and Trip-TB membrane, as shown in Table 1.

Proton Conductivity and PA Retention

The proton conductivities of PA-doped membranes were measured in-plane over the temperature range of –30 to 180 °C without humidification (Figure 3a). DMBP-TB exhibited the highest conductivity due to its highest PA uptake, while TMPI-TB/PA and Trip-TB/PA membranes also showed higher or equivalent proton conductivities than *m*-PBI/PA, despite their lower PA uptake and ADL (as shown in Table 1). This suggests that the intrinsically microporous structures in TB-based membranes likely facilitate proton transport. The highest proton conductivity of 159 mS cm^{-1} was achieved at 180 °C for DMBP-TB membranes. More importantly, we observe that the low temperature proton conductivities (from –30 to 0 °C) of TB-based PEMs were superior, and these properties are highly relevant to low temperature fuel cells and cold start-up.[15,47] We propose that the PA occupying the intrinsic micropores is responsible for higher proton conductivities at lower temperatures. In the case of DMBP-TB/PA membrane, the phenomenon was pronounced and it showed one order of magnitude higher proton conductivity (10 mS cm^{-1}) than *m*-PBI/PA (less than 1 mS cm^{-1}) (Figure 3a) at –30 °C. Additionally, we observe a similar trend for through-plane conductivities, which provides a more appropriate estimation of membrane performance in practical fuel cells (Figure S7).[48]

Since PA loss under humidified conditions is one of the major limitations for conventional *m*-PBI/PA PEMFCs, we herein used two test protocols to compare TB-based membranes and *m*-PBI to elucidate the impact of ultramicroporous structures on PA retention properties. Firstly, RH cycling experiments from 5% to 90% RH at 80 °C were performed sequentially (Figure 3b, 3c).[21] The samples were equilibrated at 5% RH for 14 h before the beginning of the next RH cycle and each RH cycle was a total of 34 h. The proton conductivity of PA-doped PEMs gradually increased with RH in all the runs[42] and *m*-PBI**/**PA achieved the highest proton conductivity at 90% RH (576 mS cm^{-1}) on the first run. However, when the second cycle started from 5% RH, an 80% reduction in proton conductivity for *m*-PBI/PA membrane was observed and the ADL value decreased from 10.5 to 4.6. In subsequent runs, under the low-RH conditions, the conductivity of *m*-PBI/PA membrane was reduced by nearly three orders of magnitude due to the excessive loss of PA, which is consistent with previous findings.[21] In contrast, for the DMBP-TB/PA membrane with ultramicroporosity, the proton conductivity progressively decreased until reaching 60% during the first five RH cycles. For the subsequent sixth and seventh runs, the conductivity exhibited little change and stabilized, implying almost no PA loss occurred during these two RH cycles. The ADL of DMBP-TB/PA membrane stabilized at about 7.5, only a 36% loss of the original PA content. This is slightly better than the QAPOH reported by Kim *et al.* (40% PA loss after five cycles under similar conditions),[21] which is one of the best PEMs having the highest PA retention properties to date. It is noteworthy that TMPI-TB/PA could not survive after the RH cycling experiments because it dissolved,

and Trip-TB/PA showed nearly no proton conductivity under low humidity (RH < 20%) and only 14.1% remaining PA after the first RH cycle. These results indicate that suitable backbone rigidity, functional group Lewis basicity, and ultramicroporosity are all crucial aspects that determine the membrane PA retention properties.

Holding the PA-doped membranes at specific temperatures and RH conditions over a long period of time is another approach to evaluate PA retention properties.[21] We selected conditions of 40 °C/60% RH and 80 °C/40% RH to determine the extent of low temperature water condensation-induced PA loss, and conditions of 160 °C/0% RH to study PA evaporation. As shown in Figure 3d-f, the PA-doped intrinsically microporous TB PEMs showed higher PA retention than that of the conventional *m*-PBI/PA membrane, no matter how harsh the conditions were. Among the TB/PA membranes, DMBP-TB with appropriate ultramicropore size and the largest FFV_3 exhibited the highest PA retention. For example, under 160 °C/0% RH conditions for 85 h, the loss of PA was only 10% for DMBP-TB/PA, while it was about 15% and 25% for Trip-TB/PA and *m*-PBI/PA membranes, respectively (Figure 3f). After 150 h exposure in 80 °C/40% RH, the PA content of *m*-PBI/PA was only 60% of the original value, while DMBP-TB/PA membrane still retained at least 89% of PA (Figure 3e). At lower temperature and under higher RH conditions (40 °C/60% RH), the PA loss of *m*-PBI/PA membranes became more serious. The proton conductivity and PA content of *m*-PBI/PA both dropped by over 50% after the 100-hour evaluation period, while those of DMBP-TB decreased by less than 20% and those of TMPI-TB/PA and Trip-TB/PA membranes decreased by 35–45% (Figure 3d). The outstanding performance of DMBP-TB/PA, which is comparable to QAPOH,[21] further verifies that the ultramicroporous TB/PA membranes with subnanometer cavities R_3 of appropriate micropore sizes can mitigate PA loss and enable operation over a full range of temperatures with enhanced water tolerance.

H_2/O_2 Fuel Cell Performance

Membrane electrode assemblies (MEAs) using PA-doped TB and *m*-PBI/PA membranes were prepared with carbon-supported Pt catalysts and polytetrafluoroethylene (PTFE) emulsion as the binder. We first evaluated different membranes at 160 °C without external humidification or backpressure, which are typical conditions employed for evaluating PA-doped membranes (Figure 4a).[49] As expected from the membrane properties, the DMBP-TB/PA-based membrane electrode assembly (MEA) achieved the best fuel cell performance, with a peak power density of 815 mW cm^{-2} at 160 °C, which is more than twice that of the MEA prepared from *m*-PBI/PA membrane (397 mW cm^{-2}, see Table S7 for a comparison of representative high-temperature PEMFC performance reported in the literature). Similar behavior was also observed for the Trip-TB/PA MEA, which demonstrated better fuel cell performance than *m*-PBI/PA, despite its lower PA uptake. The *m*-PBI/PA MEA showed the lowest performance, due to its highest cell high-frequency resistance (HFR), which increased from 224 to 254 mΩ cm^2 during the test (Figure 4a). The trend of peak power densities of these MEAs is consistent with their membrane proton conductivities as shown in Figure 3a and Figure S7. Owing to the extraordinary proton conductivity for DMBP-TB/PA membranes even at −30 °C, we then decided to extend the MEA operating temperature range without external humidification or backpressure. Surprisingly, the DMBP-TB/PA-based MEA can easily start up as low as −20 °C and can operate at a peak power density of 83 mW cm^{-2} (Figure 4b), while the *m*-PBI/PA-based MEA failed to do so due to its significantly lower proton conductivity (Figure S8). As the operating temperature increased from −20 to 160 °C, the peak power density of the DMBP-TB MEA continued to rise and the HFR decreased from 5.00 to 0.23 Ω cm^2, although no performance improvement and HFR reduction were observed when further increasing the cell temperature to 200 °C. The MEA derived from DMBP-TB/PA showed over 200 mW cm^{-2} peak power density when operating at 40 °C, while the *m*-PBI/PA-based MEA showed less than 100 mW cm^{-2} under the same conditions (Figure 4c). Therefore, the DMBP-TB/PA based MEA as a single setup can operate smoothly from −20 °C to 200 °C, which is the broadest PEMFC operating temperature range to date.

Low temperature durability tests for DMBP-TB/PA and *m*-PBI/PA-based MEAs were performed at 40 °C with H_2/O_2 and without external humidification (Figure 5a). The cell voltage of the *m*-PBI/PA MEA decreased from 0.4 V to 0.18 V within only 4 hours due to the dramatic loss of PA (Figure. S9). After the durability test, the membrane was wiped to remove any

leached PA and the residual ADL was determined to be reduced to 3.0 by acid-base titration, which corresponds to only 30% PA retention. In contrast, DMBP-TB/PA MEA showed no significant cell voltage degradation and only 5% PA loss over a period of 150 hours. Based on these results, we then evaluated the durability of DMBP-TB/PA MEAs using a more demanding accelerated stress test (AST) to investigate the PA leaching under low temperature fuel cell operating conditions.[10,50] The AST consists of shut-down and start-up cycling using a step-V procedure from 1 V to 0.1 V with a scan rate of 25 mV/min without backpressure or external humidification (Figures 5b and 5c). For the DMBP-TB/PA MEAs, the AST could be performed for over 150 cycles at both 40 °C and 15 °C, while the *m*-PBI/PA failed after only two cycles at 40 °C (Figures S10-S12). Exceptional stability was observed for the DMBP-TB/PA MEA at 15 °C, which started with 199.2 mW cm^{-2} peak power density and ADL of 10.7 and after 150 aggressive start-up/shut-down cycles, ended with 189 mW cm^{-2} peak power density (95% retention) and ADL of 9.2 (86% retention) (Figure 5b). Even at –20 °C, the AST could be carried out for more than 100 cycles, as shown in Figure 5c and Figure S11. This good performance for PA-doped, non-humidified MEAs at low temperatures further supports the enhanced PA capillary retention and cold start-up capability of the intrinsically ultramicroporous TB membranes.

Conclusion

In summary, four TB-based polymers with tunable intrinsic ultramicropores were synthesized as novel PA-doped PEMs. Fuel cells based on intrinsic microporous TB/PA PEMs were shown to be more tolerant towards water condensation owing to the delocalized effect and acid-base interactions, enabling higher PA retention and MEAs to operate at much lower temperatures than conventional PA-doped *m*-PBI PEMFCs. More specifically, the DMBP-TB/PA membranes, which had optimized ultramicroporous structure ($R \approx 3.3$ Å) and large free volume, exhibited outstanding proton conductivity and PA retention compared with other TB/PA and *m*-PBI/PA membranes. A peak power density of 815 mW cm^{-2} was achieved for DMBP-TB/PA MEA at 160°C, which was twice than that of the *m*-PBI/PA MEA. Moreover, the extraordinary properties of DMBP-TB/PA enabled the MEA to operate across a broad temperature range from − 20°C to 200°C. The low temperature performance of DMBP-TB/PA MEAs was significantly better than *m*-PBI/PA MEAs, and also outperformed PFSA-based PEMFCs, due to the non-humidified conditions and easy sub-zero start-up and operation. The ultramicroporous TB-based membranes studied herein not only bring up new strategies to solve low temperature PEMFC operation and cold-start-up issues, but also break through the classical definition of low-temperature and high-temperature PEMFCs. We believe this approach has the potential to ultimately expand PEMFC application opportunities under a broad range of environmental conditions.

Experimental Procedures

Materials

N-Methylpyrrolidone (NMP), 5(6)-amino-1,1,3-trimethyl-3-(4-aminophenyl)indan, 4,4'-methylene-bis(2-methylaniline), 4,4'-diamino-3,3'-dimethylbiphenyl, and 2,6(7)-diaminotriptycene were purchased from Aladdin. Dimethoxymethane and trifluoroacetic acid (TFA) were purchased from Energy Chemical. Phosphoric acid (PA, 85%) was purchased from Tianjin Fengchuan Fine Chemicals Co., Ltd. Dimethyl sulfoxide (DMSO), dimethylacetamide (DMAc), chloroform ($CHCl_3$), tetrahydrofuran (THF), acetone, ethanol, sodium bicarbonate ($NaHCO_3$), sodium hydroxide (NaOH) and 96% sulfuric acid (H_2SO_4) were purchased from Sinopharm Chemical Reagent Co., Ltd. All chemicals were used as received without further purification.

Synthesis of TB-polymers

For this study, four Tröger's base (TB) polymers (*i.e.*, dimethyldiphenylmethane (DMDPM-TB), dimethylbiphenyl (DMBP-TB), trimethylphenylindan (TMPI-TB), and triptycene (Trip-TB) were prepared through acid-promoted polycondensation reactions between commercially available aromatic diamine species and dimethoxymethane according to the literature

procedures.[27,36] To a 250 mL three-necked round bottom flask equipped with mechanical stirring was added a mixture of aromatic diamine (20.0 mmol) and dimethoxymethane (100 mmol), followed by cooling to 0 °C in an ice-water bath. TFA (800 mmol) was added dropwise through a constant pressure funnel at 0 °C over a 4 h period, then the reaction mixture was kept stirring at 0 °C for 24 h. After warming to ambient temperature, the reaction was allowed to stir for another 96 h. The resulting solution was precipitated in aqueous ammonium hydroxide solution, then the precipitation was filtered followed by washing with excess deionized water. The dried residue was dissolved in chloroform and precipitated in methanol, and this purification process was repeated twice. Finally, the polymer was obtained after being thoroughly dried in a vacuum oven at 50 °C for 12 h. The nuclear magnetic resonance (NMR) spectra of the resultant TB polymers matched well with previous reports, and their weight average molecular weight (M_w), number-average molecular weight (M_n) and polydispersity ($Đ$) were determined using a gel permeation chromatography (GPC) instrument equipped with a Waters 1515 isocratic HPLC pump and Waters 2414 refractive index detector (Table S1). Polystyrene standards were used for calibration and the flow rate of mobile phase (HPLC-grade tetrahydrofuran) was 0.6 mL min^{-1}.

Membrane Preparation

The TB polymers were dissolved in $CHCl_3$ (10 wt%) at room temperature. The degassed solution was cast on a glass plate and dried at room temperature for 24 h. The obtained membrane was immersed in deionized water to peel off the plate and dried in a vacuum oven at 50 °C for 12 h. All the undoped membranes had a thickness of about 80 μm.

The *m*-PBI ($M_w \approx 50$ kDa, inherent viscosity of 0.88 dL g^{-1}, 0.5 g/10 mL 96% H_2SO_4 at 30 °C), prepared according to a literature procedure[51] was dissolved in NMP to give 5 wt% solution after filtering. Then, the solution was cast on a glass substrate and the solvent was evaporated at 80 °C for 12 h in a closed oven. The obtained membrane was peeled off the substrate, and then boiled in deionized water for 12 h to remove trace amounts of NMP. Finally, the *m*-PBI membranes were obtained with a thickness of about 60 μm, after drying in a vacuum oven at 120 °C.

PA Doping

The PA-doped membranes were obtained by immersing TB membranes in PA solution at 20 °C for 0.5–8 h until their weight reached a constant value, followed by wiping with filter papers and drying in a vacuum oven at 60 °C for 2 h. All the membranes increased in thickness after PA doping. The thickness of PA doped TB membranes is about 160 mm, while that of PA doped m-PBI is about 100 mm. The PA doping level and the volume expansion measurements of the membranes were carried out in triplicate independently with different pieces of membranes to examine the reproducibility. The PA uptake and the PA-doping level were determined through acid-base titration. [38] In an ice-water bath, 0.100 M NaOH solution was used to titrate PA doped PEM samples (ca. 1 cm × 4 cm), using methyl orange as an indicator. After being neutralized, the samples were weighed (W_{dry}) after being thoroughly washed with deionized water and dried in a vacuum oven at 100 °C for 4 h. The PA uptake was calculated from the following equation:

$$\text{PA uptake (\%)} = \frac{V_{NaOH} \times C_{NaOH} \times 98.0}{Equiv_{mol} \times W_{dry}} \times 100\%$$

where V_{NaOH} (L) is the volume of NaOH used, C_{NaOH} (mol L^{-1}) is the molar concentration of NaOH, and $Equiv_{mol}$ represents the equivalent mole of titrant for PA (in this case $Equiv_{mol} = 1$), W_{dry} (g) is the dry polymer weight, and 98.0 (g mol^{-1}) is the molecular weight of PA.

The PA doping level per repeat unit (ADL) was calculated based on the following equation:

$$\text{ADL} = \frac{V_{NaOH} \times C_{NaOH} \times MW}{Equiv_{mol} \times W_{dry}}$$

where used MW (g mol^{-1}) is the molecular weight of the polymer repeat unit.

PA removal procedure

The PA saturated membranes with decided ADL were immersed in distilled water at 40 ^{o}C for 12h, and then the same procedure was repeated three times. The remaining ADL were determined again by acid-base titration using methyl orange as an indicator.

After durability test, the membrane was wiped with filter paper to remove the leaching PA. Then the content of residual acid (ADL) in the membrane was determined again by acid-base titration using methyl orange as an indicator.

Microporosity Characterization

Positron annihilation lifetime spectroscopy (PALS) was employed to determine the microcavity size and free volume in the membranes. A Positron, can form a neutral atom called a Positronium (Ps) after picking up an electron. [37] Ps has two states: the para-Ps (*p*-Ps) and the ortho-Ps (*o*-Ps). An *o*-Ps atom picks up an electron to annihilate into two photons during the collisions with the walls of free volume cavities. In polymers, the lifetime for *o*-Ps pick off annihilation usually ranges from 1 to 10 ns, which is determined by the size of the free volume cavities, and its intensity is proportional to the fraction of the free volume cavities.

The tests were performed as follows: A ^{22}Na positron source (~10 μCi) was sandwiched between two identical membrane samples with dimensions of 1.5 mm × 10 mm × 10 mm. Within a few picoseconds, a 1.28 MeV *γ*-ray was emitted by the ^{22}Na nucleus simultaneously with a positron. The time delay between the emission of the birth of the *γ*-ray (1.28 MeV) and one of the 0.511 MeV annihilation photons determines the positron lifetime. A fast-fast coincidence system served to conduct the lifetime measurements with a time resolution of ~220 ps and a channel width of 12.6 ps. The lifetime spectra were analyzed using the data processing PATFIT and CONTIN programs.

The average radius (R) of the spherical pores correlating to the *o*-Ps lifetime (t), their relative intensities (I) and the overall relative fractional free volume (FFV) within the membranes were determined by the proposed semi-empirical equations as given below:

$$\tau_{o-Ps}^{-1} = 2[1 - \frac{R}{R+\Delta R} + \frac{1}{2\pi}\sin(2\pi\frac{R}{R+\Delta R})]$$

$$FFV = C\left(\frac{4}{3}\pi R^3\right)I$$

where R represents the radius of the cavities, ΔR was obtained by empirical calibration as a constant (0.1656 nm) representing the electron layer thickness, and C is a proportionality material-dependent constant (about 0.018, which is obtained through molecular simulation).

Molecular simulation

The Molecular Dynamics (MD) simulation was constructed by the Forcite module in Materials Studio software package (Accelrys Inc., CA, USA). In one cubic simulation box, a polymer chain of 10 monomer units was used as template chain for the adjacent initial packing with the Amorphous Cell module. In every packing model four polymer chains were grown one after the other under periodic boundary conditions at 308 K and at an initial density of 0.1 g/cm^3. The density of the model will be got and the final equilibration of the packing models will be carried out with the following sequence of simulation steps: (i) 50 ps NVT-MD simulations at 600 K (a stimulated annealing), (ii) 100 ps NVT-MD simulations at 308 K (back to target temperature), (iii) 20 ps NpT-MD at 308 K and 10 bar with a timestep of 0.1 fs (for the first time volume fluctuations

are allowed in the system), followed by (iv) 280 ps NpT-MD at 308 K and 1.0 bar with a timestep of 1.0 fs, and (v) a long continuative NpT-MD simulation with the same conditions over 1 ns.

A Micromeritics ASAP 2020 instrument was used to measure N_2 adsorption/desorption of all TB polymers. Prior to gas sorption analysis, undoped samples were degassed at 393 K for 12–16 h under vacuum, while PA doped samples were degassed at 333 K for 2 h. The equilibration time was extended to 180 s to achieve the adsorption equilibrium (in the time interval, the consecutive pressure value agrees within 1.3×10^{-4} bar). BET N_2 adsorption isotherms were applied to calculate specific surface areas.

Proton Conductivity

A Bio-Logic VSP-300, FR impedance/gain phase analyzer with two-point, in-plane membrane geometry using impedance spectroscopy at frequencies ranging from 1.0 MHz to 10.0 Hz was employed to measure the proton conductivity (σ) of the PEMs. The dimensions of the sample membranes were approximately 1 cm × 4 cm and were seated between two Pt coated electrodes of a cell. An environmental chamber was used to place the testing cells with controlled atmosphere of temperature, pressure, and humidity.

The through-plane conductivity cell was constructed using platinum plated stainless steel electrolytic tank (E200, provided from Tianjin Aida Hengsheng Technology Development Co., Ltd).[48] Pt electrodes were connected to the Solartron impedance analyzer by means of pins. Prior to conducting the measurements, the cell was calibrated by measuring impedance of Nafion 211 membranes from DuPont, which were soaked in deionized water for 24 h prior to use. Membranes were cut into a circle with a diameter of 1.5 cm for the through-plane impedance measurement. The membrane sample was sandwiched between two Pt electrodes, and the cell was tightened with screws. The cell was put into the environmental chamber with controlled temperature to collect impedance data. From the following equation, the values of σ in $mS \cdot cm^{-1}$ for both cases were calculated:

$$\sigma = \frac{L}{A \times R}$$

where L is the gap between electrodes for in-plane measurements and the thickness of the membrane for through-plane measurements; A is the membrane cross-sectional area in case of the in-plane setup and the area of the electrodes in case of the through-plane setup; R is the bulk membrane resistance.

RH Cycling Experiments

The RH experiments were run sequentially by ramping up from 5% RH to 90% RH, at ~10% RH increments in an environmental chamber and at each given RH with an equilibration period of two hours. The samples were equilibrated at 5% RH for 14 h before the beginning of the next RH cycle, which was 34 h for each RH cycle. The in-plane conductivities of PEMs at 80 °C were measured every two hours and three times for each given RH, and the average was taken as the conductivity at a given RH.

The PEM strips (ca. 1 cm × 4 cm) were placed into an environmental chamber at 80 °C under 40% RH (or 180 °C with 0% RH). The changes of in-plane proton conductivity were monitored (s_t). The proton conductivity retention (R_c) of the membranes is determined by the following equation:

$$R_c\% = \frac{\sigma_t}{\sigma_i} \times 100\%$$

where s_i is the initial proton conductivity.

The stability of PA in the membranes were carried out in an environmental chamber with constant temperature and humidity for several hours. The weight of the membrane (W_i) was measured at different times and the liquid water on the surface of the membrane would be dried before weighing. The stability of PA was calculated by the weight loss ratio (R_w) of the acid in the sample, as depicted in the following equation:

$$R_w\% = \frac{W_i - W_{dry}}{W_a - W_{dry}} \times 100\%$$

where W_a is the weight of the membrane after PA doping, and W_{dry} is the weight of the membrane before PA doping.

^{31}P NMR Analysis

^{31}P-NMR spectra were recorded on a Bruker DPX-400 spectrometer at room temperature in DMSO-d_6 and were referenced to H_3PO_4 (external standard) at 0 ppm. 2 equiv PA-doped samples were obtained through adding 2 equiv 85.0% PA direct to the polymers powder. After 30 minutes of ultrasonication and a 2-hour heating at 80 ^{o}C, the mixtures were dissolved in DMSO-d_6. The PA-saturated membranes were directly dissolved in DMSO-d_6 for ^{31}P NMR spectroscopic evaluation. Solid state ^{31}P NMR spectra of the PA saturated membranes were acquired on Bruker Avance 600 MHz Wide Bore spectrometer (14.1T) using 4 mm HXY probe with ZrO_2 rotor, DR mode, lamde/2 and range coil. MAS spining rate was 9 K and chemical shifts were referenced relative to $(NH_4)_2HPO_4$, 1.00 ppm.

Single Cell Performance

Single cells with an active area of 4.0 cm^2 were used to measure the initial fuel cell performance of *m*-PBI/PA and TB/PA membranes. The MEAs for fuel cell testing were prepared by the catalyst-coated membrane (CCM) method and the catalyst layer was composed of 0.50 mg cm^{-2} Pt loading and 20 wt% PTFE content, respectively. The catalyst ink was prepared by mixing PTFE emulsion (60%) and Pt/C (40 wt%) in water-isopropanol (wt%/wt%) for 30 minutes using a magnetic stirrer, followed by ultrasonication for 30 minutes, to ensure good dispersion. The gas diffusion electrode (GDE) was prepared by painting the catalyst ink onto the carbon paper with gas diffusion layer (HCP120, from HESEN, China), and then the obtained GDE was heated at 350 °C for 30 min in a N_2 atmosphere in a tubular furnace. To fabricate the MEA, the membrane sample was sandwiched between two GDEs and then was hot-pressed at 100 °C under the pressure of 0.5 MPa. A test station (Smart 2-WonATech, Korea) was employed to study the initial fuel cell performance with no humidification and backpressure. The anode and cathode were fed with dry H_2 and O_2 at 200 sccm, respectively. The MEAs were activated at a constant voltage of 0.3 V until the current became stable. Then, steady-state polarization curves were recorded by polarizing the cell voltage from 1.0 V to 0.15 V in steps of 0.05 V, and holding the voltage for 30 s at each point. The high frequency impedance (HFR) measurement at 1 kHz was conducted when the cell reached steady state at various cell voltages using Bio-Logic VSP-300 potentiostat. The stability of PEMs was evaluated by AST. For this experiment, a shut-down and start-up cycling AST was performed via a step-V procedure from 1 V to 0.1 V with a scan rate of 50 mV/2 min, without backpressure and external humidification.

Declarations

Lead Contact

Further information and requests for resources is directed to and fulfilled by the Lead Contact, Nanwen Li (linanwen@sxicc.ac.cn).”

Materials Availability

This study did not generate new unique reagents.

Data and Code Availability

This study did not generate any datasets.

ACKNOWLEDGMENTS

We thank T.S. Yan and Z.J. He from Nankai University for the computational study the alkalinity of N atoms. We are grateful to the National Natural Science Foundation of China (No. 21835005 and No. 52G15023), Science and Technology Major Projects of Shanxi Province of China (No. 20181102019), the Hundred Talents Program of the Shanxi Province and the autonomous research project of SKLCC (Grant No.: 2020BWZ001).

SUPPLEMENTAL INFORMATION

The Supporting Information is available free of charge at XX. Curves for PALS and BET analysis, detailed PALS data, and Lewis basicity computation.

AUTHOR CONTRIBUTIONS

H.Y. Tang designed the experiments, carried out the electrochemical analysis and cell test. N.W. Li and F. Yan supervised the study. K. Geng helped for data collection. L. Wu aided in the synthesis of TB polymers. J.J. Liu and Z.Q. Chen measured the PALS of the TB membranes. H.Y. Tang, W. You, N. W. Li and M. D. Guiver drafted the manuscript with assistance from other coauthors.

DECLARATION OF INTERESTS

The authors declare no competing interests.

Received: (will be filled in by the editorial staff)

Revised: (will be filled in by the editorial staff)

Published online: (will be filled in by the editorial staff)

References

1 Devanathan, R. Recent developments in proton exchange membranes for fuel cells. *Energy Environ. Sci.* **1**, 101–119, doi: 10.1039/B808149M (2008).

2 Çelik, S. Ü., Bozkurt, A. & Hosseini, S. S. Alternatives toward proton conductive anhydrous membranes for fuel cells: Heterocyclic protogenic solvents comprising polymer electrolytes. *Prog. Polym. Sci.* **37**, 1265–1291, doi: 10.1016/j.progpolymsci.2011.11.006 (2012).

3 Mauritz, K. A. & Moore, R. B. State of understanding of Nafion. *Chem. Rev.* **104**, 4535–4585, doi: 10.1021/cr0207123 (2004).

4 Zhang, J. *et al.* High temperature PEM fuel cells. *J. Power Sources* **160**, 872–891, doi: 10.1016/j.jpowsour.2006.05.034 (2006).

5 Zhu, Y., Zhu, W. H. & Tatarchuk, B. J. Performance comparison between high temperature and traditional proton exchange membrane fuel cell stacks using electrochemical impedance spectroscopy. *J. Power Sources* **256**, 250–257, doi: 10.1016/j.jpowsour.2014.01.049 (2014).

6 Schmidt, T. J. & Baurmeister, J. Durability and reliability in high-temperature reformed hydrogen PEFCs. *ECS Transactions* **3**, 861–869, doi: 10.1149/1.2356204 (2006).

7 Bose, S. *et al.* Polymer membranes for high temperature proton exchange membrane fuel cell: Recent advances and challenges. *Prog. Polym. Sci.* **36**, 813–843, doi: 10.1016/j.progpolymsci.2011.01.003 (2011).

8 Li, Q., Jensen, J. O., Savinell, R. F. & Bjerrum, N. J. High temperature proton exchange membranes based on polybenzimidazoles for fuel cells. *Prog. Polym. Sci.* **34**, 449–477, doi: 10.1016/j.progpolymsci.2008.12.003 (2009).

9 Ma, Y. L., Wainright, J. S., Litt, M. H. & Savinell, R. F. Conductivity of PBI membranes for high-temperature polymer electrolyte fuel cells. *J. Electrochem. Soc.* **151**, A8–A16, doi: 10.1149/1.1630037 (2004).

10 Yu, S., Xiao, L. & Benicewicz, B. C. Durability studies of PBI-based high temperature PEMFCs. *Fuel Cells* **8**, 165–174, doi: 10.1002/fuce.200800024 (2008).

11 Li, Q., He, R., Jensen, J. O. & Bjerrum, N. J. PBI-based polymer membranes for high temperature fuel cells – Preparation, characterization and fuel cell demonstration. *Fuel cells* **4**, 147–158, doi: 10.1002/fuce.200400020 (2004).

12 Xiao, L. *et al.* High-temperature polybenzimidazole fuel cell membranes via a sol-gel process. *Chem. Mater.* **17**, 5328–5333, doi: 10.1021/cm050831 (2005).

13 Kim, J., Kim, M., Lee, B.-G. & Sohn, Y.-J. Durability of high temperature polymer electrolyte membrane fuel cells in daily based start/stop operation mode using reformed gas. *Int. J. Hydrogen Energy* **40**, 7769–7776, doi: 10.1016/j.ijhydene.2014.12.122 (2015).

14 Lang, S., Kazdal, T. J., Kühl, F. & Hampe, M. J. Experimental investigation and numerical simulation of the electrolyte loss in a HT-PEM fuel cell. *Int. J. Hydrogen Energy* **40**, 1163–1172, doi: 10.1016/j.ijhydene.2014.11.041 (2015).

15 Wei, L., Liao, Z., Suo, Z., Chen, X. & Jiang, F. Numerical study of cold start performance of proton exchange membrane fuel cell with coolant circulation. *Int. J. Hydrogen Energy* **44**, 22160–22172, doi: 10.1016/j.ijhydene.2019.06.147 (2019).

16 Oszcipok, M. *et al.* Portable proton exchange membrane fuel-cell systems for outdoor applications. *J. Power Sources* **157**, 666–673, doi: 10.1016/j.jpowsour.2006.01.005 (2006).

17 Amamou, A. A., Kelouwani, S., Boulon, L. & Agbossou, K. A Comprehensive review of solutions and strategies for cold start of automotive proton exchange membrane fuel cells. *IEEE Access* **4**, 4989–5002, doi: 10.1109/access.2016.2597058 (2016).

18 Maruo, T. *et al.* Development of fuel cell system control for sub-zero ambient conditions. *SAE Technical Paper Series*, doi:10.4271/2017-01-1189 (2017).

19 Jiang, W., Song, K., Zheng, B., Xu, Y. & Fang, R. Study on fast cold start-up method of proton exchange membrane fuel cell based on electric heating technology. *Energies* **13**, 4456|1–26, doi: 10.3390/en13174456 (2020).

20 Wen, J. *et al.* Alternate hydrogen pump method enables start-up from −30°C for graphite-bipolar-plate proton exchange membrane fuel cells. *J. Electrochem. Soc.* **166**, F1112–F1116, doi: 10.1149/2.0091914jes (2019).

21 Lee, K.-S., Spendelow, J. S., Choe, Y.-K., Fujimoto, C. & Kim, Y. S. An Operationally flexible fuel cell based on quaternary ammonium-biphosphate ion pairs. *Nat. Energy* **1**, 16120|1–7, doi: 10.1038/nenergy.2016.120 (2016).

22 Lee, K.-S. *et al.* Intermediate temperature fuel cells via an ion-pair coordinated polymer electrolyte. *Energy Environ. Sci.* **11**, 979–987, doi: 10.1039/C7EE03595K (2018).

23 Lee, A. S., Choe, Y.-K., Matanovic, I. & Kim, Y. S. The energetics of phosphoric acid interactions reveals a new acid loss mechanism. *J. Mater. Chem. A* **7**, 9867–9876, doi: 10.1039/c9ta01756a (2019).

24 Atanasov, V. *et al.* Synergistically integrated phosphonated poly(pentafluorostyrene) for fuel cells. *Nat. Mater.*, **20**, p370–377; doi: 10.1038/s41563-020-00841-z (2021).

25 McKeown, N. B. & Budd, P. M. Polymers of intrinsic microporosity (PIMs): Organic materials for membrane separations, heterogeneous catalysis and hydrogen storage. *Chem. Soc. Rev.* **35**, 675–683, doi: 10.1039/b600349d (2006).

26 Carta, M. *et al.* An efficient polymer molecular sieve for membrane gas separations. *Science* **339**, 303–307, doi: 10.1126/science.1228032 (2013).

27 Xu, Z., Liao, J., Tang, H., Efome, J. E. & Li, N. Preparation and antifouling property improvement of Tröger's base polymer ultrafiltration membrane. *J. Membr. Sci.* **561**, 59–68, doi: 10.1016/j.memsci.2018.05.042 (2018).

28 Zuo, P. *et al.* Sulfonated Microporous polymer membranes with fast and selective ion transport for electrochemical energy conversion and storage. *Angew. Chem. Int. Ed.* **59**, 9564–9573, doi: 10.1002/anie.202000012 (2020).

29 Yang, Z. *et al.* Highly conductive anion-exchange membranes from microporous Tröger's base polymers. *Angew. Chem. Int. Ed.* **55**, 11499–11502, doi: 10.1002/anie.201605916 (2016).

30 Tan, R. *et al.* Hydrophilic microporous membranes for selective ion separation and flow-battery energy storage. *Nat. Mater.* **19**, 195–202, doi: 10.1038/s41563-019-0536-8 (2020).

31 Patel, H. A. *et al.* Proton conduction in Tröger's base-linked poly(crown ether)s. *ACS Appl. Mater. Interfaces* **10**, 25303–25310, doi: 10.1021/acsami.8b05532 (2018).

32 Ma, X. *et al.* Facile synthesis and study of microporous catalytic arene-norbornene annulation–Tröger's base ladder polymers for membrane air separation. *ACS Macro Lett.* **9**, 680–685, doi: 10.1021/acsmacrolett.0c00135 (2020).

33 Liu, X. *et al.* Oriented proton-conductive nano-sponge-facilitated polymer electrolyte membranes. *Energy Environ. Sci.* **13**, 297–309, doi: 10.1039/c9ee03301g (2020).

34 Zhou, S. *et al.* Alkaline polymers of intrinsic microporosity: high-conduction and low-loss anhydrous proton exchange membranes for energy conversion. *J. Mater. Chem. A* **9**, 3925–3930, doi: 10.1039/d0ta12100b (2021).

35 Zhang, E. *et al.* NMR analysis of phosphoric acid distribution in porous fuel cell catalysts. *Chem. Commun.* **57**, 2547–2550, doi: 10.1039/d0cc07738k (2021).

36 Carta, M. *et al.* The synthesis of microporous polymers using Tröger's base formation. *Polym. Chem.* **5**, 5267–5272, doi: 10.1039/c4py00609g (2014).

37 Liao, K.-S. *et al.* Determination of free-volume properties in polymers without orthopositronium components in positron annihilation lifetime spectroscopy. *Macromolecules* **44**, 6818–6826, doi: 10.1021/ma201324k (2011).

38 Provencher, S. W. Contin: A general purpose constrained regularization program for inverting noisy linear algebraic and integral equations. *Comput. Phys. Commun.* **27**, 229–242, doi: 10.1016/0010-4655(82)90174-6 (1982).

39 Kirkegaard, P., Eldrup, M., Mogensen, O. E. & Pedersen, N. J. Program system for analysing positron lifetime spectra and angular correlation curves. *Comput. Phys. Commun.* **23**, 307–335, doi: 10.1016/0010-4655(81)90006-0 (1981).

40 Thommes, M. Physical adsorption characterization of nanoporous materials. *Chem. Ing. Tech.* **82**, 1059–1073, doi: 10.1002/cite.201000064 (2010).

41 Sebastiani, D. Current densities and nucleus-independent chemical shift maps from reciprocal-space density functional perturbation theory calculations. *ChemPhysChem* **7**, 164–175, doi: 10.1002/cphc.200500438 (2006).

42 Aihara, Y., Sonai, A., Hattori, M. & Hayamizu, K. Ion conduction mechanisms and thermal properties of hydrated and anhydrous phosphoric acids studied with ^{1}H, ^{2}H, and ^{31}P NMR. *J. Phys. Chem. B* **110**, 24999–25006, doi: 10.1021/jp064452v (2006).

43 Xu, Z., Shi, J. L., Chen, X. & Jiang, X. K. ^{31}P NMR study on some phosphorus-containing compounds. *Chinese Chem. Lett.* **11**, 1057–1060, doi: (2000).

44 Guo, S.-Y., Guo, Q.-H., Tong, S. & Wang, M.-X. Synthesis of electron-deficient corona[5]arenes and their selective complexation with dihydrogen phosphate: Cooperative effects of anion-pi interactions. *Angew. Chem. Int. Ed.* **132**, 8155–8160, doi: 10.1002/anie.201915839 (2020).

45 Harris, R. K., Thompson, T. V., Norman, P. R. & Pottage, C. Adsorption competition onto activated carbon, studied by magic-angle spinning NMR. *Journal of the Chemical Society, Faraday Transactions* **92**, 2615–2618, doi: 10.1039/FT9969202615 (1996).

46 Dickinson, L. M., Harris, R. K., Shaw, J. A., Chinn, M. & Norman, P. R. Oxygen-17 and deuterium NMR investigation into the adsorption of water on activated carbon. *Magnetic Resonance in Chemistry* **38**, 918–924, doi: 10.1002/1097-458X(200011)38:11<918::AID-MRC749>3.0.CO;2-7 (2000).

47 Uosaki, K., Okazaki, K. & Kita, H. Conductivity of Nafion membranes at low temperatures. *J. Electroanal. Chem. Interfacial Electrochem.* **287**, 163–169, doi: n.a. (1990).

48 Soboleva, T. *et al.* Investigation of the through-plane impedance technique for evaluation of anisotropy of proton conducting polymer membranes. *J. Electroanal. Chem.* **622**, 145–152, doi: 10.1016/j.jelechem.2008.05.017 (2008).

49 Aili, D. *et al.* Thermal curing of PBI membranes for high temperature PEM fuel cells. *J. Mater. Chem.* **22**, 5444–5453, doi: 10.1039/c2jm14774b (2012).

50 Haider, R. *et al.* High temperature proton exchange membrane fuel cells: progress in advanced materials and key technologies. *Chem. Soc. Rev.*, **50**, 1138-1187; doi: 10.1039/d0cs00296h (2021).

51 Yang, J. S. *et al.* High molecular weight polybenzimidazole membranes for high temperature PEMFC. *Fuel Cells* **14**, 7–15, doi: 10.1002/fuce.201300070 (2014).

Figures

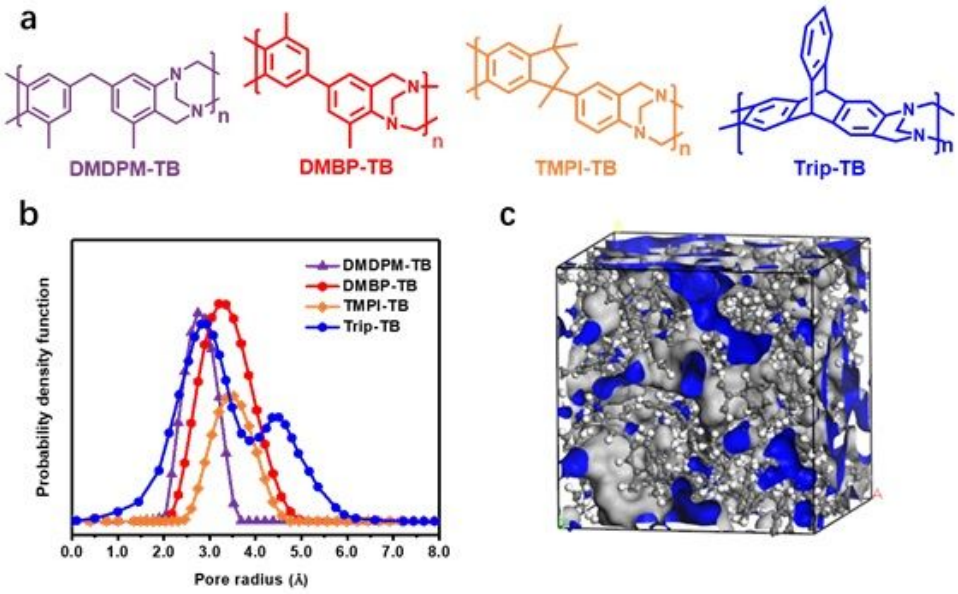

Figure 1

(a) Structures of four different TB polymers. (b) Pore size distributions obtained via CONTIN analysis from PALS. (c) 3D view of DMBP-TB modelled structure in an amorphous cell.

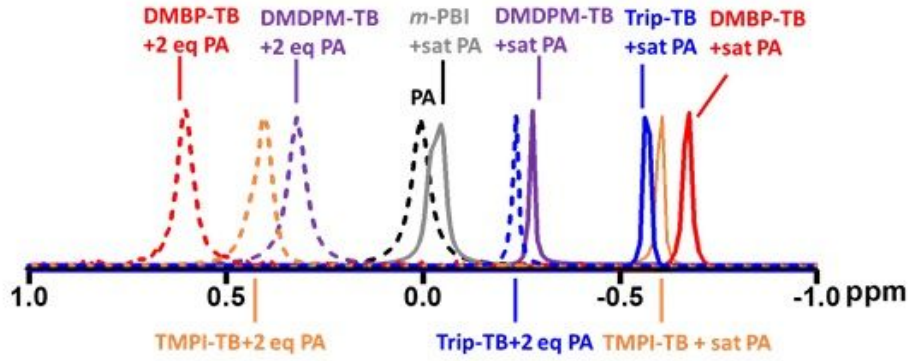

Figure 2

31P NMR spectra of PA-doped TB membranes in DMSO-d6.

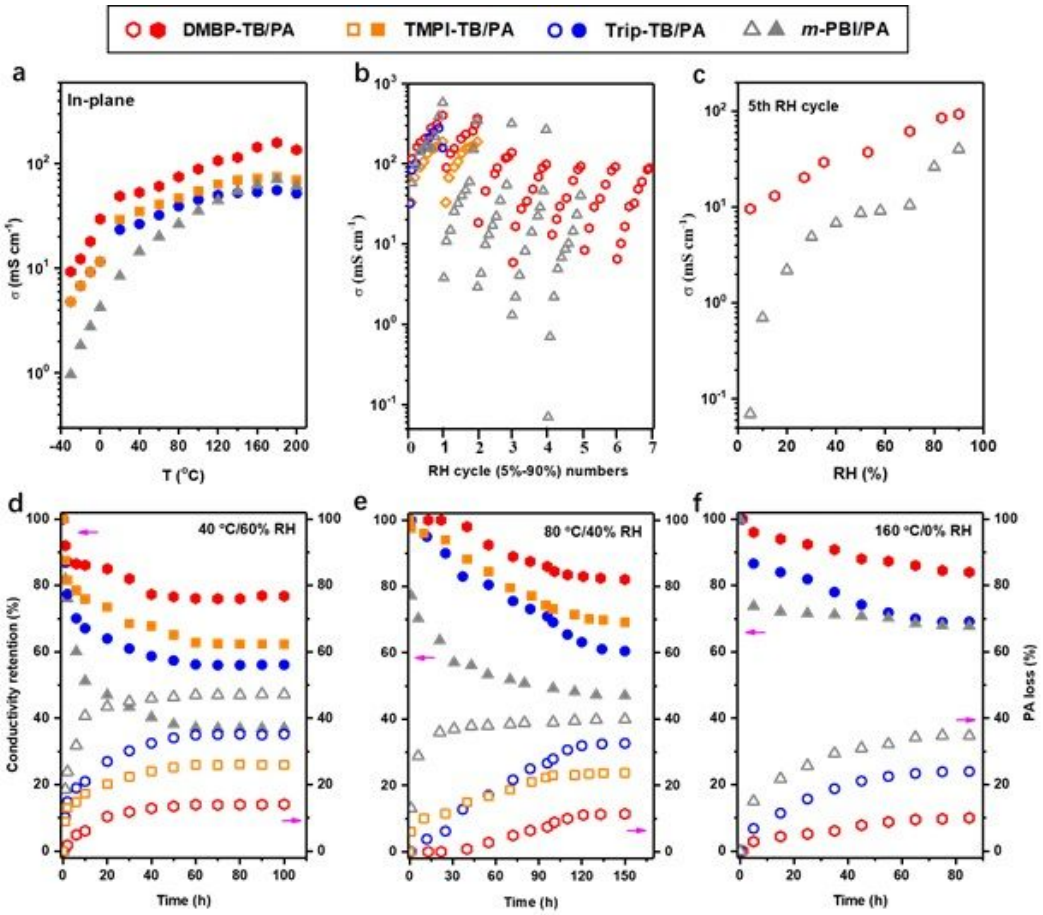

Figure 3

a) Temperature-dependent in-plane proton conductivity of PA-doped PEMs without humidification. b) Changes in in-plane proton conductivity at 80 °C were measured at different RH by ramping sequentially from 5% to 90% with ~10% RH increments for PA-doped PEMs. After 90% RH, the RH was reduced to 5% RH, and equilibrated for 14 h before the next cycle began. c), Changes in in-plane proton conductivity at 80 °C in the 5th RH cycle. d) e) and f) Conductivity and PA loss for PA-doped membranes as a function of time at 40 °C/60% RH, 80 °C/40% RH, and 160 °C/0% RH respectively.

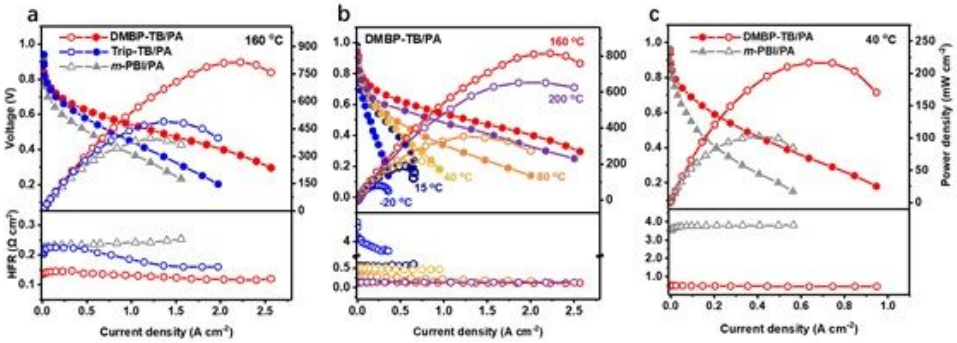

Figure 4

i-V curves, power density and HFR of MEAs without backpressure nor external humidification. a) TB/PA and m-PBI/PA MEAs at 160 °C; b) DMBP-TB/PA MEAs as a function of operating temperature; c) DMBP-TB/PA and m-PBI/PA MEAs at 40 °C. Testing conditions: Anode/Cathode: Pt/C (0.50 mg Pt cm−2), PTFE binder (20 wt%), H2/O2 flow: 200 sccm. Data represented by the filled symbols in the panel refer to the voltage. PEM thickness: TB/PA membranes 160 μm, m-PBI/PA membrane 100 μm.

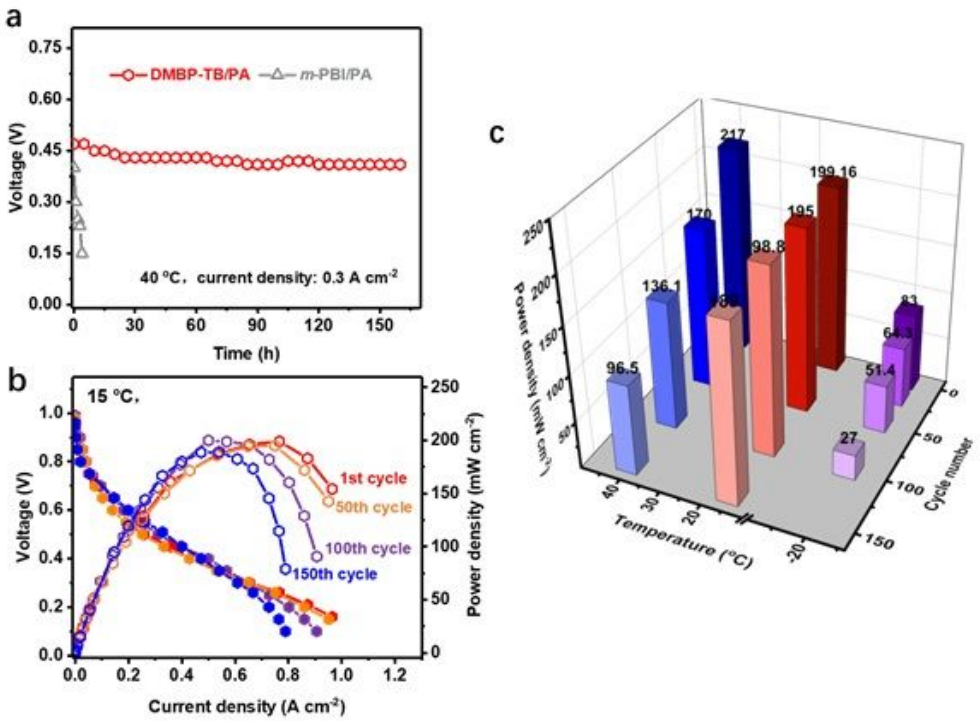

Figure 5

a) Durability of DMBP-TB/PA and m-PBI/PA MEAs at 40 °C; b) i-V curves of the shut-down and start-up AST cycling tests for the DMBP-TB/PA MEA at 15 °C; and c) Peak power density values of the DMBP-TB/PA MEAs after the shut-down/start-up AST cycling at −20 °C, 15 °C, and 40 °C. Testing conditions: Anode/Cathode: Pt/C (0.50 mg Pt cm−2), PTFE binder (20 wt%), H2/O2 flow: 200 sccm, without back pressure. Data represented by the filled symbols in the panel refer to the voltage, PEM thickness: TB/PA membranes about 160 μm, m-PBI/PA membrane 100 μm.

Supplementary Files

This is a list of supplementary files associated with this preprint. Click to download.

- ESI.docx